

Multiphoton excitation and high harmonic generation in rectangular graphene quantum dot

A G Ghazaryan* and Kh V Sedrakian

Centre of Strong Fields Physics, Yerevan State University, 1 A. Manukian, Yerevan 0025, Armenia

E-mail: amarkos@ysu.am

27 September 2022

Abstract. The multiphoton excitation and high harmonic generation (HHG) processes are considered using the microscopic quantum theory of nonlinear interaction of strong coherent electromagnetic (EM) radiation with rectangular graphene quantum dot (RGQD). The dynamic Hartree-Fock approximation is developed for the consideration of the quantum dot-laser field nonlinear interaction at the nonadiabatic multiphoton excitation regime. The many-body Coulomb interaction is described in the extended Hubbard approximation. By numerical results, we show the significance of the RGQD lateral size, shape, and EM wavefield orientation in RGQD of the zigzag edge compared to the armchair edge in the HHG process allowing for increasing the cutoff photon energy and the quantum yield of higher harmonics.

1. Introduction

The quantum electrodynamic phenomena caused by the strong coherent EM radiation, such as multiphoton HHG and related processes, through nonlinear channels in two-dimensional (2D) atomic systems-nanostructures are of great interest in lowenergy physics and nanooptoelectronics due to the unique physical properties of such 2D nanosystems of atomic thickness [1–9]. It was been studied systematically the HHG in bulk crystals [10–16] and low-dimensional nanostructures such as graphene and its derivatives [17–39], monolayer transition metal dichalcogenides [40–42], hexagonal boron nitride [43], topological insulator [44], [45], monolayers of black phosphorus [46], curved 2D hexagonal nanostructures [47], solids [48], [49], as well as in other 2D systems [50–52]. 2D nanosystems enable the development of important technological applications [53]. The quantum cascade laser is one such example [54], using physical phenomena in 2D systems such as the quantum Hall effect [8].

As a nonlinear medium, the graphene quantum dot (GQD) [53], [55–58], and such as graphene nanoribbon [1], [59–70], are of particular interest. These can be closed and convex structures such as fullerenes of various basic symmetry, as well as plane structures of various lateral sizes, shapes, edges, and doping levels [59–61]. As known,

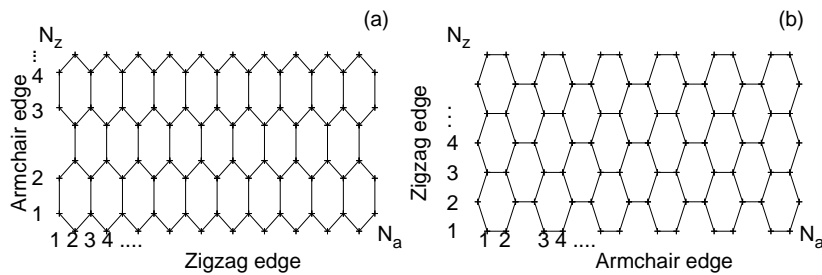


Figure 1. The geometrical structure of $(N_a; N_z)$ -sized RGQD with $N = N_a N_z$ atoms. (a) shows RGQD with zigzag edge along the x axis with $N = 84$ atoms for $N_a = 21$; $N_z = 4$, (b) – RGQD with armchair edge along the x axis for $N_a = 12$; $N_z = 7$. The distance between nearest neighboring atoms is $b \simeq 1.42 \text{ \AA}$.

the symmetry of the graphene sublattice in GQD can be controlled by the lateral size, shape, and type of the GQD edge [57–72]. The behavior of GQD is quantitatively different for nanostructures with zigzag and armchair edge [73], [74]. Thus, GQDs have richer electronic properties than graphene unbounded in space [75–77]. Moreover, they are of particular interest because their nonlinear optical properties can be controlled [1].

The 2D graphene unbounded in space formed in the type of a narrow ribbon leads to the confinement of carriers in quasi-one-dimensional graphene nanoribbons (with different topologies depending on the shape of the ribbon) [26]. An important advantage of GQD over graphene nanoribbons [69], [78–80] is the complete confinement of quasiparticles in space. For a bounded quantum system, due to the lack of translational symmetry, the spectrum only consists of a discrete set of energy levels, not bands. One of the advantages of limited quantum systems is the ability to change their energy spectra and wavefunctions by adjusting their size [81], [82] or external parameters such as gate voltage or magnetic field [83–85]. Note that the HHG spectra in GQDs can be affected by the constraint conditions — the lateral size of the dot and/or the coupling parameters in the bounded GQDs [67], [57], [58]. The HHG efficiency is expected to increase with increasing confinement since the latter will limit the propagation of the electron wave packet [86].

In the present paper, we consider the multiphoton HHG in the RGQD–plane quasi-zero-dimensional GQD of the rectangular shape [87–89], with zigzag and armchair edges on the elongated side of the different lateral sizes induced by intense coherent radiation in the nonlinear regime. The many-body Coulomb interaction is taken into account in the extended Hubbard approach [60, 61], [90]. Note that the considered GQDs, where the engineering of optoelectronic properties is allowed, currently are accessible in practice [59], [68]. A closed system of differential equations for a single-particle density matrix at the multiphoton interaction of RGQD with a strong laser field is solved numerically.

The paper is organized as follows. In Sec. II, we consider multiphoton excitation

and HHG in RGQD of the different lateral sizes, laser intensity, and polarization of the wave field. The comparison with the case of the armchair edge on the elonged side of RGQD was done. Conclusions are given in Sec. III. Finally, in Sec. IV the set of equations for the single-particle density matrix has been formulated, taking into account the many-body Coulomb interaction.

2. Basic model, numerical results and discussions

We will study in RGQD the HHG of the plane quasi-monochromatic EM wave of linear polarization, propagating perpendicular to the xy plane, with homogeneous quasi-periodic electric field strength:

$$\mathbf{E}(t) = \hat{\mathbf{e}} E_0 f(t) \cos \omega t, \quad (1)$$

where $\hat{\mathbf{e}}$ is the unit polarization vector in the xy plane, E_0 and ω respectively are the amplitude and carrier frequency, $f(t) = \sin^2(\pi t/\mathcal{T})$ is the slowly changing envelope, $\mathcal{T} = 40\pi/\omega$ is the impulse duration. Fig. 1 shows the geometric structure of the zero-dimensional RGQD in xy plane. There are N_a and N_z carbon atoms along the x axis and the y axis, respectively. All carbon atoms are packed into a hexagonal lattice. The total number of carbon atoms RGQD is $N = N_a N_z$. Note that, for nanoribbons with a limited armchair edge width, the electronic structure and energy spectrum of quasiparticles for $N_a \gg N_z$ and $N_a \ll N_z$, when the RGQD will be similar to a nanoribbon, critically depend on the width of the RGQD along the y axis and the width along the x axis, respectively [70]. In relation to [70], we have the insulator case of RGQD (Fig. 1).

Thus, we will use the microscopic nonlinear quantum theory of the HHG process in the strong EM wave in RGQD by the tight-binding model (TB) [59], [91] for the Hamiltonian \hat{H} , taking into account the Coulomb interaction in the generalized Hubbard approximation. The total Hamiltonian by the empirical TB model [91] is given in Sec. IV. Using numerical diagonalization, we will find the eigenstates $\psi_\mu(i)$ and eigenenergies ε_μ ($\mu = 0, 1 \dots N-1$). The results of numerical diagonalization are shown in Fig. 2 for the different lateral sizes and edges of RGQD. As shown in Fig. 2, without the tunneling all energy levels have degenerated. It can also be seen from Fig. 2 that the density of states increases with an increase in the number of lattice atoms. As will be seen later, this directly affects the yield of HHG.

The basic theory is given in Seq. Appendixes. The quantum dynamics of RGQD in a strong EM wave with periodic excitation is determined by a closed system of differential equations (11) for the density matrix, which must be solved with the certain initial conditions. We construct mainly the density matrix $\rho_{0ij}^{(\sigma)}$ through the filling of electronic states in valence band in accordance with the Fermi–Dirac distribution at zero temperature

$$\rho_{0ij}^{(\sigma)} = \sum_{\mu=N/2}^{N-1} \psi_\mu^*(j) \psi_\mu(i), \quad (2)$$

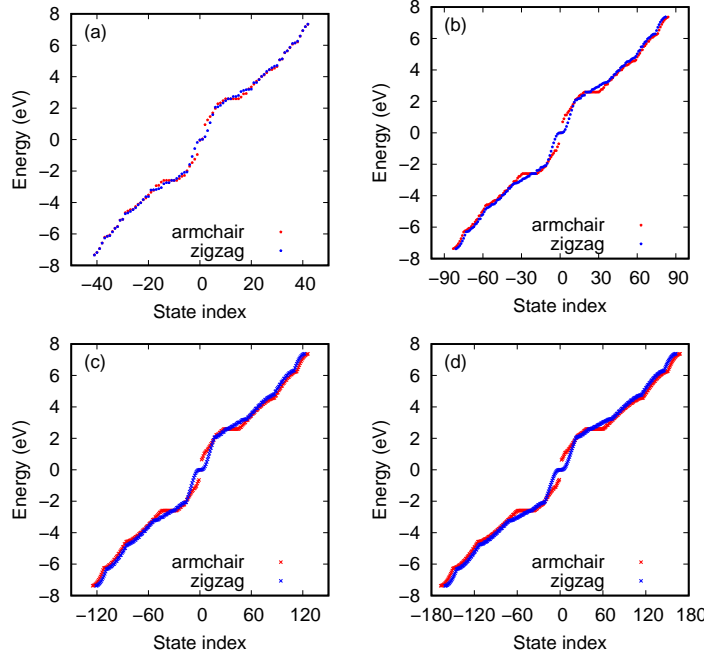


Figure 2. (Color online) The eigenenergies in RGQD. (a–d) for zigzag edge along the x axis respectively correspond to $N = 84(N_a = 21), 164(N_a = 41), 244(N_a = 61), 324(N_a = 81)$, atoms; and $N_z = 4$ for all cases. The same for RGQD of armchair edge along the x axis for (a–d) $N = 84(N_a = 12), 168(N_a = 24), 252(N_a = 36), 336(N_a = 48)$ atoms, respectively; and $N_z = 7$ for all cases.

with an eigenstate $\psi_\mu(i)$ of the Hamiltonian \hat{H}_0 (9). For the density matrix we solve numerically by integration the equations of motion Eq. 11 over time with the standard fourth-order Runge-Kutta algorithm.

The emission spectrum of harmonics is defined by the Fourier transform $\mathbf{a}(\Omega)$ of the dipole acceleration:

$$\mathbf{a}(t) = d^2 \mathbf{d} / dt^2. \quad (3)$$

The dipole momentum is:

$$\mathbf{d}(t) = \left\langle \sum_{i\sigma} \mathbf{r}_i c_{i\sigma}^\dagger c_{i\sigma} \right\rangle, \quad (4)$$

normalized by the number N of lattice atoms, and the factor $a_0 = \bar{\omega}^2 d_0$, where $\bar{\omega} = 1 \text{ eV}/\hbar$ and $d_0 = 1 \text{ \AA}$. The power emitted at a given frequency is proportional to $|\mathbf{a}(\Omega)|^2$. We introduce the angle θ between the polarization vector $\hat{\mathbf{e}} = \{\cos \theta, \sin \theta\}$ and the x axis directed by the alonged edge (see Fig. 1). The relaxation rate is taken $\hbar\gamma = 50 \text{ meV}$. The electron-electron interaction (EEI) energy of on-site Coulomb repulsion is $U \simeq 3 \text{ eV}$ (see in Sec. IV). The inter-site Coulomb repulsion energy is taken $V \simeq 0.9 \text{ eV}$. The energy between the nearest-neighbor atoms is $t_{ij} = 2.7 \text{ eV}$. To clarify the main aspects of multiphoton HHG in RGQD, we assume that the excitation frequency is $\omega = 0.1 \text{ eV}/\hbar$, which is much smaller than the typical scales t_{ij}, U, V .

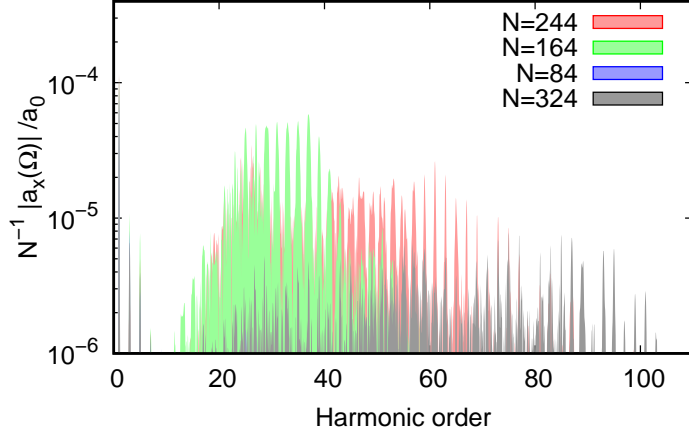


Figure 3. (Color online) The HHG emission spectra in the strong-field regime via dipole acceleration Fourier transformation $N^{-1}|a_x(\Omega)|/a_0$ (in arbitrary units) versus the harmonic number for RGQD with zigzag edge on the elongated side of different number N of atoms. The relaxation rate is $\hbar\gamma = 50$ meV. The linearly polarized wave frequency is $\omega = 0.1$ eV/ \hbar and wavefield strength is $E_0 = 0.1$ V/ \AA at fixed angle $\theta = 0$. The spectra are shown for moderate typical EEI energies: $U = 3$ eV, $V = 0.9$ eV.

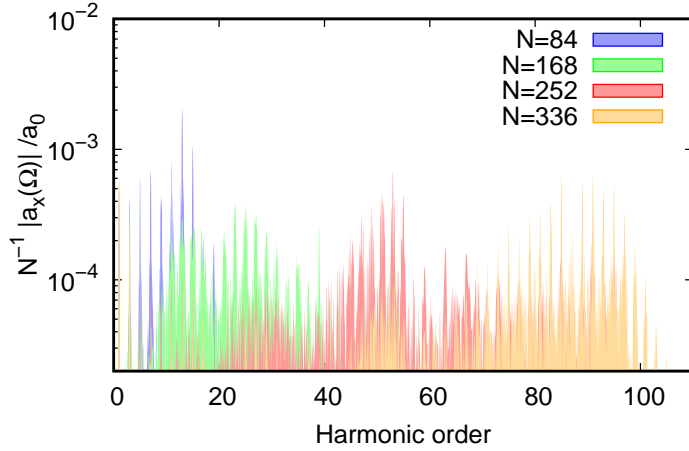


Figure 4. (Color online) The same as for Fig. 3 but for RGQD of armchair edge along the x axis.

Next, we will consider the origin of the HHG in the quantum dot. There are two contributions to the current: the electron/hole transitions within unoccupied/occupied states and the electron-hole creation (transitions from occupied states to unoccupied ones) and subsequent recombination. The first transitions make a contribution only to low harmonics and is analogous to the intraband current in a semiconductor, while the latter makes the main contribution in the high-frequency part corresponding to the interband current, which represents recombination/creation of electron-hole pairs. This picture is analogous to HHG in solid-state systems. To separate these contributions in the dipole acceleration spectrum we made a change of the basis via formula $\rho_{ij} = \sum_{\mu'} \sum_{\mu} \psi_{\mu'}^*(j) \rho_{\mu\mu'} \psi_{\mu}(i)$, where $\rho_{\mu\mu'}$ is the density matrix in the energetic

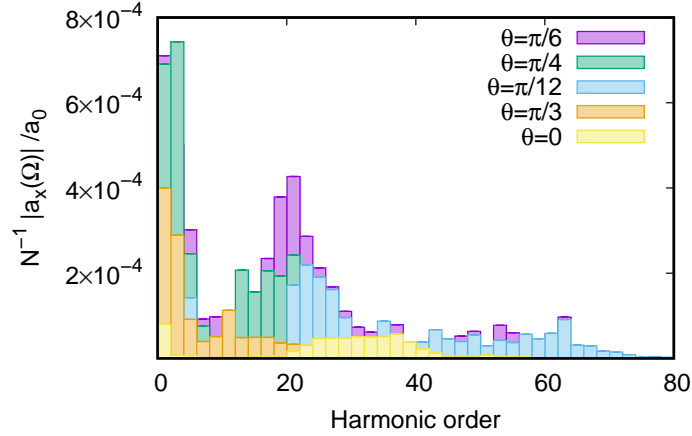


Figure 5. (Color online) The same as for Fig. 3 but for different angles θ composed between in-plane electric field and x axis for $N = 164$ atoms of RGQD.

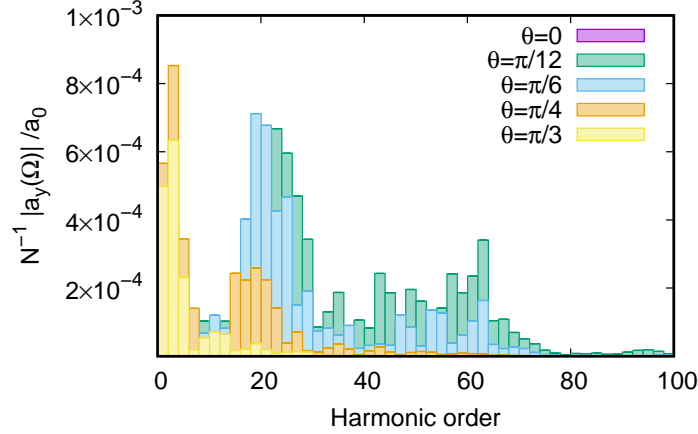


Figure 6. (Color online) The same as for Fig. 5 but for a_y -component.

representation. Hence intraband part of dipole acceleration defines as

$$\mathbf{d}_{\text{intra}}(t) = \sum_{\mu, \mu'=N/2}^{N-1} \rho_{\mu\mu'}(t) \mathbf{d}_{\mu'\mu} + \sum_{\mu, \mu'=0}^{N/2-1} \rho_{\mu\mu'}(t) \mathbf{d}_{\mu'\mu}, \quad (5)$$

and interband part will be

$$\mathbf{d}_{\text{inter}}(t) = 2 \sum_{\mu'=N/2}^{N-1} \sum_{\mu=0}^{N/2-1} \text{Re} \rho_{\mu\mu'}(t) \mathbf{d}_{\mu'\mu}, \quad (6)$$

where dipole transition matrix elements are:

$$\mathbf{d}_{\mu'\mu} = \sum_i \psi_{\mu'}^*(i) \mathbf{r}_i \psi_{\mu}(i). \quad (7)$$

In the following we will consider two contributions intraband (5) and interband (6), to the total current numerically.

In Figs. 3, 4 the HHG spectrum determined by $|a_x(\Omega)|$ is presented in RGQD of the different lateral sizes of correspondently zigzag and armchair edge on the elongated

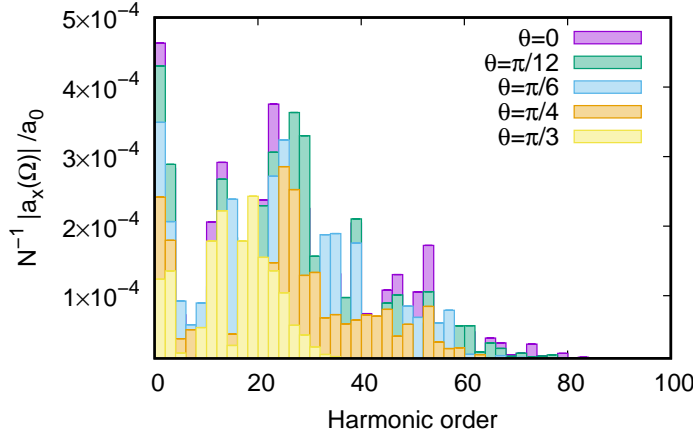


Figure 7. (Color online) The same as for Fig. 5 but for $N = 168$ atoms of RGQD of armchair edge along the x axis.

side. The linearly polarized EM wavefield is taken at polarization angle $\theta = 0$, $E_0 = 0.1$ V/Å, $\omega = 0.1$ eV/ \hbar . The EEI energies are $U \simeq 3$ eV, $V \simeq 0.9$ eV. As expected, the appearance of odd harmonics in the HHG spectrum is associated with the conservation of inversion symmetry in RGQD, as in ordinary graphene [1], [56]. This is a result of the interference of the two different contributions, intraband (5) and interband (6). In Figs. 3, 4 we see the typical nonperturbative behavior of HHG spectra with a multiple plateau structure. In these cases, the dominant plateau shifted towards higher frequencies with an increase in the number of atoms. In particular, as shown in Fig. 3, at $N = 164$, $N = 244$, and $N = 324$ we have an effective generation of harmonics from the 10th to the 60th, the 20th to the 90th, and from the 20th to the 100th, respectively. When, as shown in Fig. 4, in RGQD of armchair edge in RGQD, in particular for $N = 168$ and $N = 336$, we have an efficient generation of harmonics from 10th to 40th and 70th to 100th, respectively. This is related to the energy spectrums in Fig. 2, in which, with an increase in the number of lattice atoms, new higher energy states with an increasing density of states appear. As shown in Figs. 3 and 4, there are main differences in the higher harmonics spectra for the close lateral size RGQDs of different edges on the elonged sides. Thus, the HHG spectra maxima and cutoff energies are different in RGQDs of zigzag and armchair edges on the elonged sides. As will be shown by the following (see Fig. 14, red bar), for RGQD at some angles $\theta > 0$ the magnitudes of high-order harmonics in the elonged zigzag case can become larger than at the armchair edge case, especially for a_y .

Furthermore, RGQD also has a strong anisotropic nonlinear response, depending on the orientation of the EM wavefield relative to the elonged side [57], [58]. For RGQD at $\theta = 0$ and $\theta = \pi/2$, the harmonic polarization direction coincides with the incident wave polarization direction. At other angles $0 < \theta < \pi/2$, harmonics appear with polarization vectors perpendicular to the pump wavefield. To reveal the dependence of the HHG spectra on the orientation of the EM wavefield in Figs. 5 and 6 show the

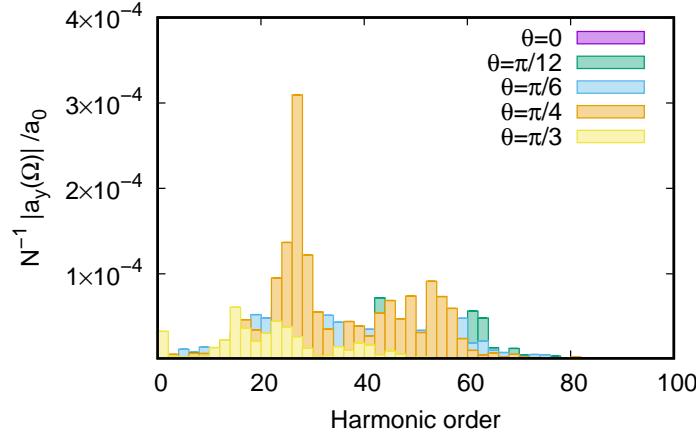


Figure 8. (Color online) The same as for Fig. 7 but for a_y -component.

HHG spectra for different θ of the pump wavefield relative to the x axis in the RGQD of zigzag edge for $N = 164$, for $|a_x|$ and $|a_y|$ components, respectively. In contradistinction to the isotropic HHG spectrum for unbounded in space graphene at the low-frequency pump wave, the spectrum is anisotropic at a high-frequency wave, when, due to the symmetry of the carbon hexagonal cell, the optical response with respect to the driven field polarization is periodic with a period of $\pi/3$ [92]. For the RGQD we have strong anisotropy. In particular, for HHG process in the case of more than the first eight harmonics for the y component the angles $\pi/12 \lesssim \theta \lesssim \pi/6$ are preferable, while for the x -component we have a maximum for the angle $\pi/6$. Moreover, different polarization angles lead to different maxima in the harmonic spectra and cutoff energies. In Figs. 7, 8 the same is shown for RGQD of armchair edge. For this case we see a completely different picture. In particular, for the x -component the angles $0 \lesssim \theta \lesssim \pi/12$ are preferable, meanwhile for the y -component we have a maximum near the angle $\theta \sim \pi/4$. The latter is also a consequent of the rich spectra of eigenstates in Fig. 2 with different symmetry. Note that during the generation process, only odd harmonics appear in the RGQD, regardless of its orientation. This is due to the inversion symmetry of the sublattice of RGQD.

Next, we consider the HHG spectra depending on the intensity of the pump wave. Fig. 9 (a) shows the HHG spectra via the field strength and the harmonic order for a fixed frequency and EEI energies $U = 3$ eV, $V \simeq 0.9$ eV in RGQD of zigzag elonged edge with $N = 164$ atoms. We will mention, that for HHG it is important to increase the HHG emission efficiency and increase the harmonic cutoff threshold. As shown in Fig. 9 (a), within each plateau, the cutoff harmonic increases linearly with increasing wavefield strength. Then, reaching harmonics $n_{\text{cut}} \simeq 110$. Note that the linear dependence of the cutoff harmonics on the wave intensity is similar to HHG through discrete levels [93–95], or in crystals with linear energy dispersion [45], [96]. To compare in Fig. 9 (b) we show the same for RGQD of the armchair edge on the elongated side. Fig. 9 has demonstrated the same multi-plateau behavior. Many differences appear in Fig. 9 (a)

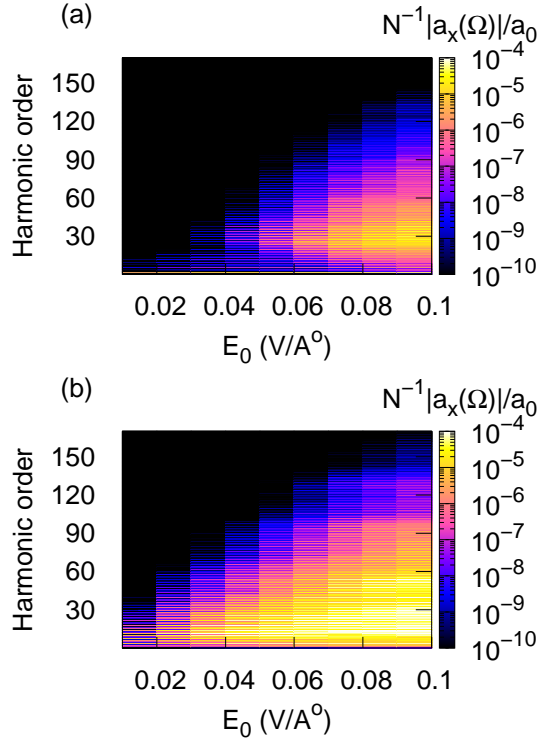


Figure 9. (Color online) The color bars represent the HHG emission rate in strong field regime in the logarithmic scale via dipole acceleration Fourier transformation $N^{-1}|a_x(\Omega)|/a_0$ (in arbitrary units) versus harmonic order and the wavefield strength E_0 , at fixed angle $\theta = 0$ for (a) $N = 164$ at zigzag edge and (b) $N = 168$ at armchair edge of RGQD on the elongated side. The wave frequency is $\omega = 0.1$ eV/ \hbar and the EEI energies are $U = 3$ eV and $V \simeq 0.9$ eV. The relaxation rate is $\hbar\gamma = 50$ meV.

and (b), in particular, the absence of the rates of harmonic orders less $n = 30$ in Fig. 9 (a), depending on the dipole momentum transition matrix elements (4) in the RGQD of the zigzag or armchair edges are defined by the internal static property of the system of the quantum dot.

To reveal such differences via edge on the elongated side of the RGQD for different lateral sizes, in Figs. 10 and 11 was shown the x -component of the dipole momentum $|\mathbf{d}_{\mu'\mu}|$ (7) via the eigenstate index difference and energy difference (transition energy), correspondently demonstrated for a zigzag and armchair edges. In Figs. 10, 11 appear, that with a change in the state index, new higher energy states with an increasing density of states appear, and the states are strongly different for zigzag and armchair edges of RGQD (connecting with different topologies depending on the edge on the elongated side of the quantum dot). As it is shown in Figs. 10, 11, with the growth in the number of carbon atoms the corresponding HHG rates related by the transitions with the more significant change of the state index occur relating to interband transitions, moreover, it prevails in the case of armchair edge. Despite this, as shown in Fig. 10, 11 for (c-f), in both cases of RGQD edges, the energy difference of transitions tends to saturation with the increasing number of carbon atoms.

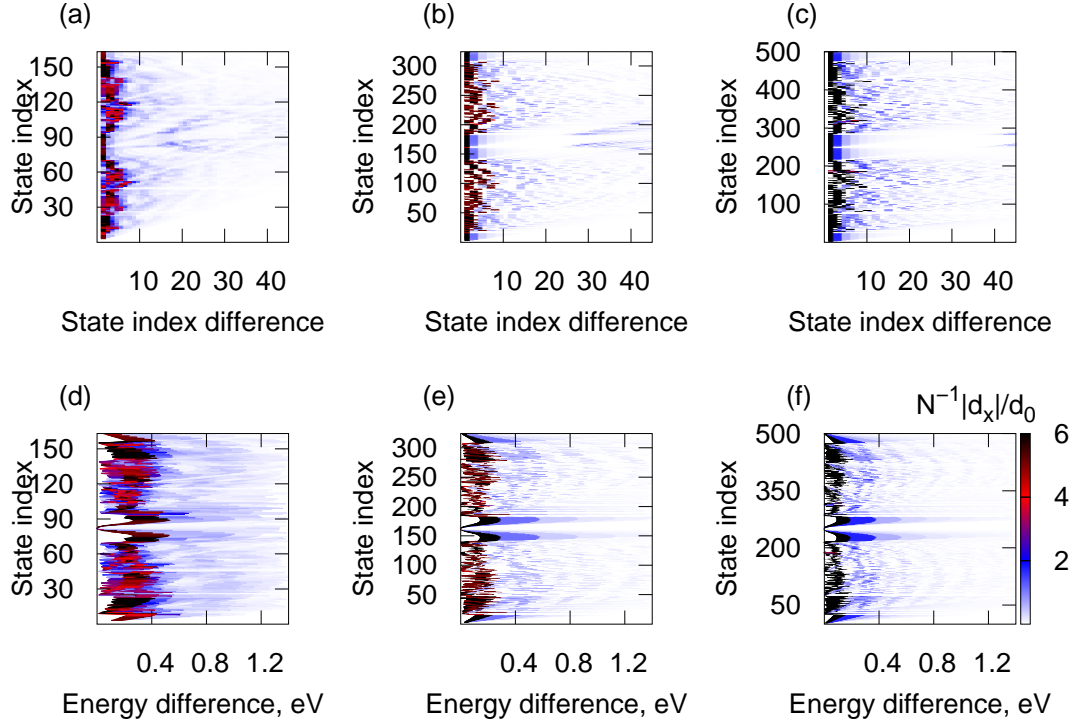


Figure 10. (Color online) The color bars represent the dipole momenta in the logarithmic scale $N^{-1}|d_x|/d_0$ (in arbitrary units) versus eigenstate index difference and state index. (a–c) respectively correspond to $N = 164, 324, 500$ atoms of RGQD with a zigzag edge along the x axis. (d–f) show the same but versus eigenstate energy difference and state index.

Is in the particular interest the dipole momentum y -component. The transitions, relating with d_y , appear mainly due to the strong coherent EM radiation. In Figs. 12, 13 d_y -components are shown for different edges and atom numbers of RGQD. As Figs. 12 and 13 show, that although the d_y -component by an order of magnitude is smaller than the d_x -component, the HHG rates are defined by correspondent transitions between eigenstates with higher index difference, than in the case of d_x -component; and for the RGQD of the armchair edge, the dipole momentum magnitude is larger than in the case of zigzag edge on the elonged side. In contradiction with Fig. 13 of the quantum dot of the elonged armchair edge, in Fig. 12 for the zigzag edge, the middle isolated lines corresponding to the substantial increase in the magnitude of d_y -component is clearly visible, which due to interband transitions (defined by respective state index difference). The latter has the main contribution to the high-frequency part corresponding to the interband current, which is connected with recombination/creation of electron-hole pairs, and it will correspondently increase the HHG rates. Moreover, Figs. 12, 13 for (d–f) show the satiation of the dipole momentum magnitude depending on the state energy difference with the atom number growth, as in Figs. 10, 11 for (d–f).

In relation to the mentioned, Fig. 14 shows the high harmonic spectrum versus the angle θ of the EM wavefield relative to the elonged side, and harmonic order. (a) and (c)

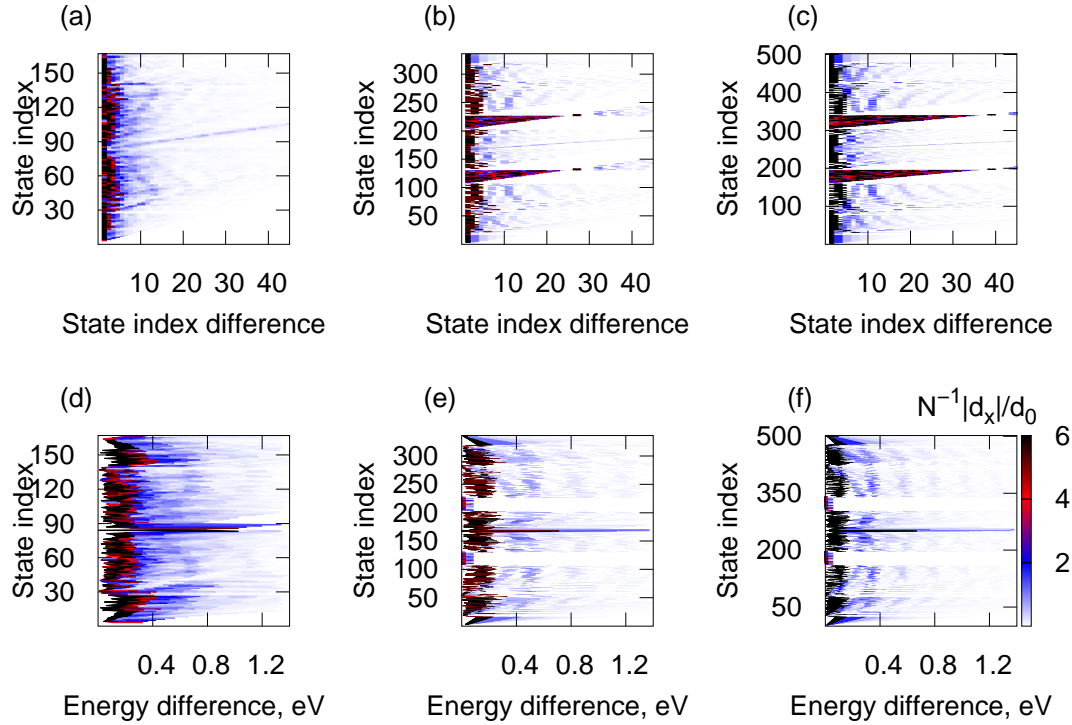


Figure 11. (Color online) The same as for Fig. 10 but for RGQD with an armchair edge for (a–c), as for as (d–f), corresponding to $N = 168, 336, 504$ atoms, respectively.

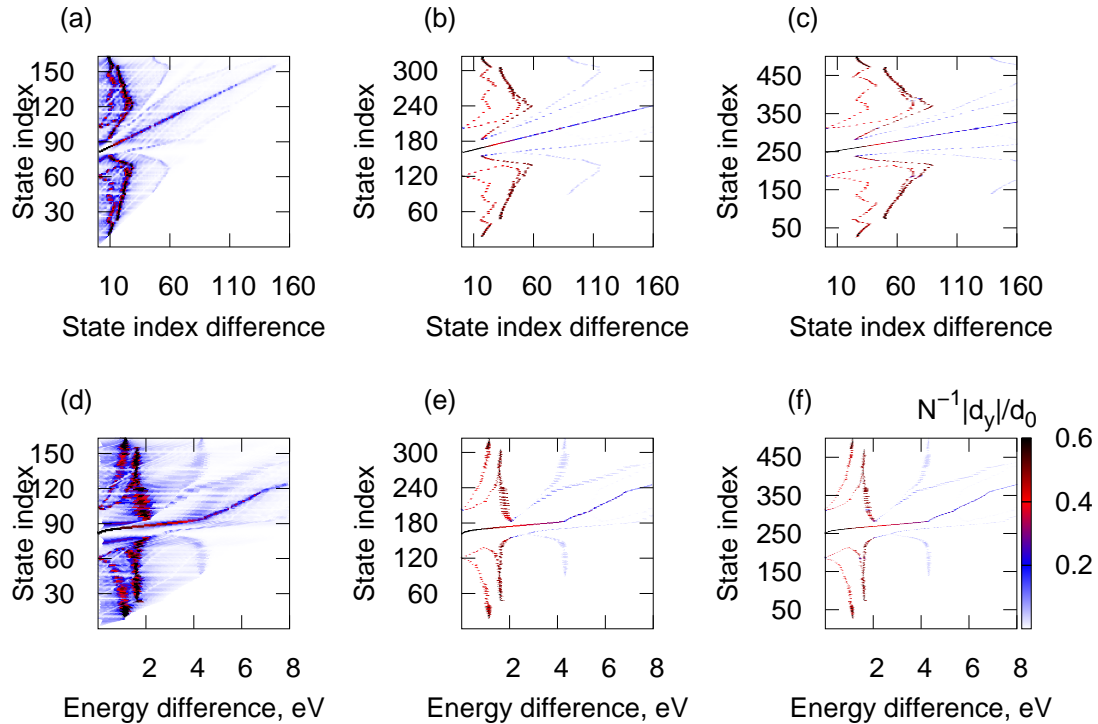


Figure 12. (Color online) The same as for Fig. 10 but for d_y -component.

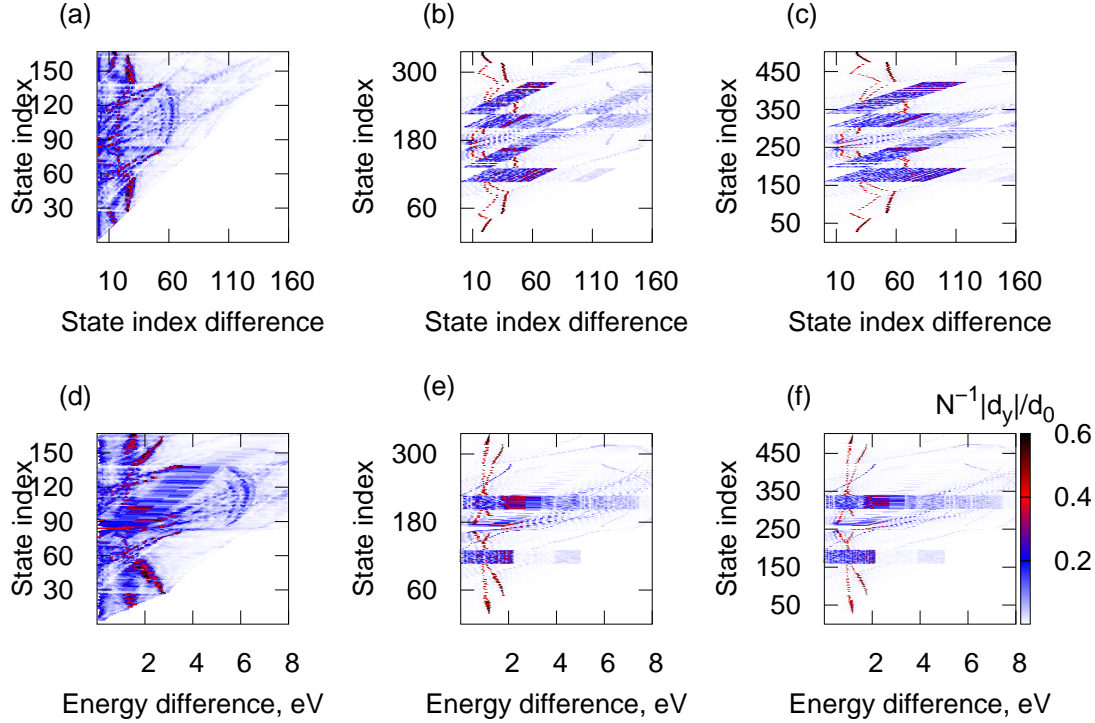


Figure 13. (Color online) The same as for Fig. 11 but for d_y -component.

are demonstrated $|a_x|$ and $|a_y|$, respectively, in RGQD of zigzag edge on the elonged side. (b) and (d) correspond $|a_x|$ and $|a_y|$, respectively, in RGQD of armchair edge. Fig. 14 is demonstrated for $n = 120$ harmonic numbers in accordance with the energystate index range $(-120, 120)$ in Fig. 2 (c) for correspondent number of atoms. As shown in Fig. 14, in contradistinction to the RGQD with an armchair edge, in the case of a zigzag edge on the elonged side of RGQD, if for the y -component we have maxima (red and black dots) in the high-frequency part of HHG corresponding to transitions from occupied states to unoccupied ones (the electron-hole creation and subsequent recombination), meanwhile for the x -component the preferable angles (in accordance with Fig. 5–8) appear in the low-frequency part of HHG spectra for the electron/hole transitions between nearest-neighbor eigenstates (within unoccupied/occupied states). Former transitions correspond to the interband current, which represents the recombination/creation of electron-hole pairs, while the latter corresponds to the intraband current. As shown in Fig. 14, that is defined by respective state energy difference $n\hbar\omega$. The interband current sufficiently enhances the HHG process rate in the elonged zigzag edge case.

3. Conclusion

We have investigated the generation of infrared laser field harmonics in the extreme nonlinear strong field regime on the RGQD of different lateral sizes and edges. We treated the system evolution in the strong laser field on the basis of the Hartree-Fock

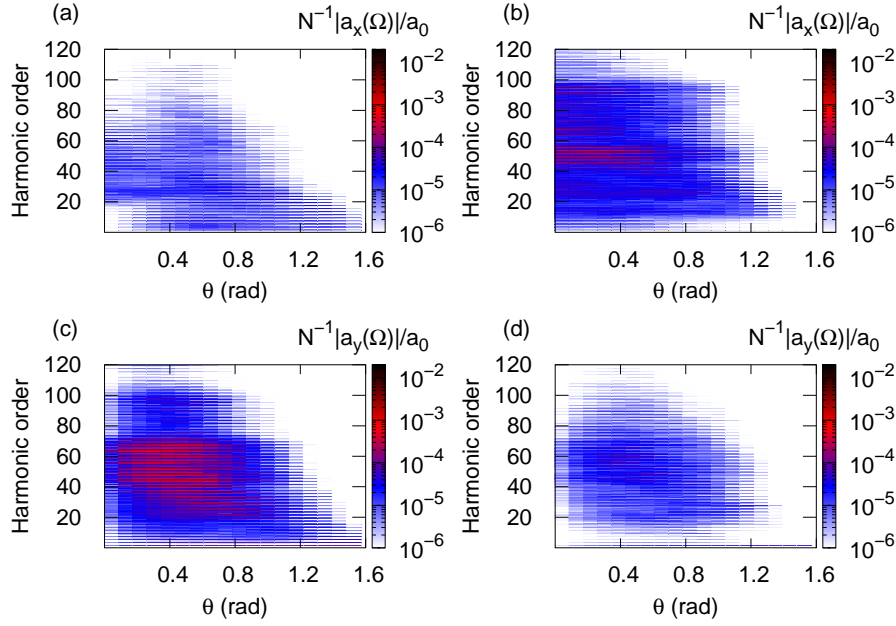


Figure 14. (Color online) The color bars represent the HHG emission rate in strong field regime in the logarithmic scale via dipole acceleration Fourier transformation $N^{-1}|a_i(\Omega)|/a_0$ (in arbitrary units, $i = x, y$) versus θ and harmonic order for (a) $N = 244$ at zigzag edge and (b) $N = 252$ at armchair edge of RGQD. The wavefield strength is $E_0 = 0.1$ V/Å with frequency $\omega = 0.1$ eV/ \hbar , and the EEI energies are $U = 3$ eV and $V \simeq 0.9$ eV. The relaxation rate is taken $\hbar\gamma = 50$ meV.

approximation. The multiparticle Coulomb interaction we consider in the extended Hubbard approximation. The numerical results revealed the typical non-perturbative multiple-plateaus of the spectrum of HHG, the boundaries of which are determined by the internal excitation lines of the dot, and the differences related to the RGQD edge. Note, that the dominant plateau shifted towards higher frequencies with an increase in the number of atoms. Therefore, by changing the lateral size of the nanostructure, it is possible to increase the orders of harmonics within the main plateau. In addition, the cutoff photon energy also shifts toward blue with an increase in the transverse size of the nanostructure. We have shown that the HHG spectra have a strong anisotropy depending on the orientation of the electromagnetic wave field strength relative to the RGQD zigzag edge on the elonged side. Different polarization angles lead to different maxima in the harmonic spectra and cutoff energies. The isolated line corresponds to mainly an increase in the dipole momentum y -the component that appears in the HHG process on RGQD along the zigzag edge, which causes a sufficient increase in the high-order harmonics yield. The obtained results show that RGQD can serve as a medium for HHG at interacting with a strong laser field, for the appearance of new energy states, including that HHG probability increases with growth in the number of dot atoms. This can be a proper way to enhance the quantum yield of the HHG and the energy of photons in this process on the graphene-like quantum dots.

4. Appendixes: Interaction Hamiltonian

Here we will present the total Hamiltonian by the empirical TB model [91] in the form:

$$\hat{H} = \hat{H}_0 + \hat{H}_{\text{int}}, \quad (8)$$

where

$$\hat{H}_0 = \frac{1}{2} \sum_{\langle i,j \rangle} V_{ij} n_i n_j + \frac{U}{2} \sum_{i\sigma} n_{i\sigma} n_{i\bar{\sigma}} - \sum_{\langle i,j \rangle \sigma} t_{ij} c_{i\sigma}^\dagger c_{j\sigma}. \quad (9)$$

is the free RGQD Hamiltonian. Here $c_{i\sigma}^\dagger$ is the operator of creation of an electron with spin polarization $\sigma = (\uparrow, \downarrow)$ at site i , and $\langle i, j \rangle$ is the summation over nearest neighbor sites with the transfer energy t_{ij} ($\bar{\sigma}$ is the opposite to spin polarization); and $n_{i\sigma} = c_{i\sigma}^\dagger c_{i\sigma}$ is the electron density operator with total electron density for the site i : $n_i = n_{i\uparrow} + n_{i\downarrow}$. The first and the second terms in free Hamiltonian (9) correspond to the EEI within the extended Hubbard approximation (\hat{H}_{ee}) with inter-site $\sim V_{ij}$ and on-site $\sim U$ Coulomb repulsion energies. The inter-site Coulomb repulsion is described by the distance d_{ij} between the nearest-neighbour pairs varied over the system: $\sim V_{ij} = V d_{\min}/d_{ij}$ (d_{\min} is the the minimal nearest-neighbor distance). For the all calculations we have taken $V = 0.3U$ [97], [98]. The third term in (9) is the kinetic energy part of the TB Hamiltonian with tunneling matrix element t_{ij} neighboring sites. The hopping integral t_{ij} between the nearest-neighbor atoms of GQDs can be determined experimentally, and is usually taken to be $t_{ij} = 2.7$ eV [1]. Note, that we neglected the lattice vibrations in the Hamiltonian.

The laser-RGQD interaction is described in the length-gauge via the pure scalar potential:

$$\hat{H}_{\text{int}} = e \sum_{i\sigma} \mathbf{r}_i \mathbf{E}(t) c_{i\sigma}^\dagger c_{i\sigma},$$

where \mathbf{r}_i is the position vector, e is the elementary charge. We will obtain evolutionary equations for the single-particle density matrix $\rho_{ij}^{(\sigma)} = \langle c_{j\sigma}^\dagger c_{i\sigma} \rangle$ from the Heisenberg equation $i\hbar \partial \hat{L} / \partial t = [\hat{L}, \hat{H}]$. Let us the system relaxes at a rate γ to the equilibrium $\rho_{0ij}^{(\sigma)}$ distribution. The EEI will be considered under the Hartree-Fock approximation, and to describe a closed set of equations for the single-particle density matrix $\rho_{ij}^{(\sigma)}$, we will assumed the Hamiltonian (9) in the form:

$$\begin{aligned} \hat{H}_0^{HF} \simeq & - \sum_{\langle i,j \rangle \sigma} t_{ij} c_{i\sigma}^\dagger c_{j\sigma} + U \sum_i (\bar{n}_{i\uparrow} - \bar{n}_{0i\uparrow}) n_{i\downarrow} \\ & + U \sum_{i\sigma} (\bar{n}_{i\downarrow} - \bar{n}_{0i\downarrow}) n_{i\uparrow} + \sum_{\langle i,j \rangle} V_{ij} (\bar{n}_j - \bar{n}_{0j}) n_i \\ & - \sum_{\langle i,j \rangle \sigma} V_{ij} c_{i\sigma}^\dagger c_{j\sigma} \left(\langle c_{i\sigma}^\dagger c_{j\sigma} \rangle - \langle c_{i\sigma}^\dagger c_{j\sigma} \rangle_0 \right), \end{aligned} \quad (10)$$

with $\bar{n}_{i\sigma} = \langle c_{i\sigma}^\dagger c_{i\sigma} \rangle = \rho_{ii}^{(\sigma)}$. Thus, the following equation for the density matrix is obtained:

$$i\hbar \frac{\partial \rho_{ij}^{(\sigma)}}{\partial t} = \sum_k \left(\tau_{kj\sigma} \rho_{ik}^{(\sigma)} - \tau_{ik\sigma} \rho_{kj}^{(\sigma)} \right) + (V_{i\sigma} - V_{j\sigma}) \rho_{ij}^{(\sigma)} + e\mathbf{E}(t) (\mathbf{r}_i - \mathbf{r}_j) \rho_{ij}^{(\sigma)} - i\hbar\gamma \left(\rho_{ij}^{(\sigma)} - \rho_{0ij}^{(\sigma)} \right), \quad (11)$$

and the matrixes $V_{i\sigma}$, $\tau_{ij\sigma}$ are approximated by the density matrix $\partial \rho_{ij}^{(\sigma)}$:

$$V_{i\sigma} = \sum_{j\alpha} V_{ij} \left(\rho_{jj}^{(\alpha)} - \rho_{0jj}^{(\alpha)} \right) + U \left(\rho_{ii}^{(\bar{\sigma})} - \rho_{0ii}^{(\bar{\sigma})} \right), \quad (12)$$

$$\tau_{ij\sigma} = t_{ij} + V_{ij} \left(\rho_{ji}^{(\sigma)} - \rho_{0ji}^{(\sigma)} \right). \quad (13)$$

In this representation, the initial value of density matrix $\langle c_{i\sigma}^\dagger c_{j\sigma} \rangle_0$ is defined via TB Hamiltonian $\hat{H}_0^{TB} = -\sum_{\langle i,j \rangle \sigma} t_{ij} c_{i\sigma}^\dagger c_{j\sigma}$. We will numerically diagonalize the TB Hamiltonian \hat{H}_0 . That is, in the static limit the Hartree-Fock Hamiltonian vanishes $\hat{H}_{ee}^{HF} \simeq 0$, and the EEI in Hartree-Fock limit is included in empirical hopping integral between the nearest-neighbor atom t_{ij} which is chosen to be close to experimental data [59]. Thus, the EEI in the Hartree-Fock approximation is correspond only for quantum dynamics initiated by the pump laser field.

The authors are deeply grateful to prof. H. K. Avetissian and Dr. G. F. Mkrtchian for permanent discussions and valuable recommendations. This work was supported by the Science Committee of RA in Frames of Project 21AG-1C014.

References

- [1] Novoselov K S, Geim A K, Morozov S V at el. 2004 *Science* **306** 666
- [2] Geim A K 2009 *Science* **324** 1530
- [3] Castro Neto A H, Guinea F, Peres N M R at el. 2009 *Rev. Mod. Phys.* **81** 109
- [4] Brabec T and Krausz F 2000 *Rev. Mod. Phys.* **72** 545
- [5] Corkum P B 1993 *Phys. Rev. Lett.* **71** 1994
- [6] Agostini P and DiMauro L F 2004 *Rep. Prog. Phys.* **67** 813
- [7] Kohler M C, Pfeifer T, Hatsagortsyan K Z, Keitel C H 2012 *Adv. Atom. Mol. Opt. Phys.* **61** 159
- [8] Avetissian H K 2016 *Relativistic Nonlinear Electrodynamics: The QED Vacuum and Matter in Super-Strong Radiation Fields* (New York: Springer)
- [9] Ferray M, L'Huillier A, Li X F, Lompre L A at el. 1988 *Journal of Physics B* **21** L31
- [10] Ghimire S, DiChiara A D, Sistrunk E at el. 2011 *Nature Physics* **7** 138
- [11] Schubert O, Hohenleutner M, Langer F at el. 2014 *Nature Photonics* **8** 119
- [12] Vampa G, Hammond T J, Thire N at el. 2015 *Nature* **522** 462
- [13] Ndabashimiye G, Ghimire S, Wu M at el. A 2016 *Nature* **534** 520
- [14] You Y S, Reis D A, and Ghimire S 2017 *Nature Physics* **13** 345349
- [15] Liu H, Guo C, Vampa G at el. 2018 *Nature Physics* **14** 1006
- [16] Avetissian H K, Avetisyan V N, Avchyan B R, Mkrtchian G F 2022 *Phys. Rev. A* **106** 033107
- [17] Mikhailov S A and Ziegler K 2008 *J. Phys. Condens. Matter* **20** 384204
- [18] Avetissian H K, Avetissian A K, Mkrtchian G F, Sedrakian Kh V 2012 *Phys. Rev. B* **85** 115443

- [19] Avetissian H K, Avetissian A K, Mkrtchian G F, Sedrakian Kh V 2012 *J. Nanophoton.* **6** 061702
- [20] Avetissian H K, Mkrtchian G F, Batrakov K G at el. 2013 *Phys. Rev. B* **88** 165411
- [21] Bowlan P, Martinez-Moreno E, Reimann K at el. 2014 *Phys. Rev. B* **89** 041408
- [22] Al-Naib I, Sipe J E, and Dignam M M 2015 *New J.Phys.* **17** 113018
- [23] Chizhova L A, Libisch F, and Burgdorfer J 2016 *Phys. Rev. B* **94** 075412
- [24] Avetissian H K and Mkrtchian G F 2016 *Phys. Rev. B* **94** 045419
- [25] Avetissian H K, Ghazaryan A G, Mkrtchian G F, Sedrakian Kh V 2017 *J. Nanophoton.* **11** 016004
- [26] Avetissian H K, Avchyan B R, Mkrtchian G M, Sargsyan K A 2020 *J. Nanophoton.* **14** 026018
- [27] Chizhova L A, Libisch F, and Burgdorfer J 2017 *Phys. Rev. B* **95** 085436
- [28] Dimitrovski D, Madsen L B, and Pedersen T G 2017 *Phys. Rev. B* **95** 035405
- [29] Yoshikawa N, Tamaya T, and Tanaka K 2017 *Science* **356** 736
- [30] Golub A, Egger R, Muller C, and Villalba-Chavez S 2020 *Phys. Rev. Lett* **124** 110403
- [31] Avetissian H K and Mkrtchian G F 2018 *Phys. Rev. B* **97** 115454
- [32] Avetissian A K, Ghazaryan A G, Sedrakian Kh V 2019 *J. Nanophoton.* **13(3)** 036010
- [33] Ghazaryan A G, Sedrakian Kh V 2019 *J. Nanophoton.* **13(4)** 046004
- [34] Ghazaryan A G, Sedrakian Kh V 2019 *J. Nanophoton.* **13(4)** 046008
- [35] Avetissian A K, Ghazaryan A G, Sedrakian Kh V, Avchyan B R 2017 *J. Nanophoton.* **11** 036004
- [36] Avetissian A K, Ghazaryan A G, Sedrakian Kh V, Avchyan B R 2018 *J. Nanophoton.* **12** 016006
- [37] Avetissian H K, Avetissian A K, Ghazaryan A G at el. 2020 *J. Nanophoton.* **14** 026004
- [38] Avetissian H K, Avetissian A K, Avchian B R, and Mkrtchian G F 2019 *Phys. Rev. B* **100** 035434
- [39] Bludov Yu, Peres N, M. Vasilevskiy M 2020 *Phys. Rev. B* **101** 075415
- [40] Liu H, Li Y, You Y S at el. 2017 *Nature Physics* **13** 262
- [41] Mkrtchian G F, Knorr A, and Selig M, 2020 *Phys. Rev. B* **100**125401
- [42] Avetissian H K, Mkrtchian G F, Hatsagortsyan K Z 2020 *Phys. Rev. Research* **2** 023072
- [43] Breton G Le, Rubio A, Tancogne-Dejean N 2018 *Phys. Rev. B* **98** 165308
- [44] Avetissian H K, Avetissian A K, Avchyan B R, Mkrtchian G F 2018 *J. Phys. Condens. Matter* **30** 185302
- [45] Avetissian H K, Avetissian A K, Avchyan B R, Mkrtchian G F 2019 *Phys. Rev. B* **100** 035434
- [46] Pedersen T G 2017 *Phys. Rev. B* **95** 235419
- [47] Avetissian H K and Mkrtchian G F 2019 *Phys. Rev. B* **99** 085432
- [48] Almalki S, Parks A M, Bart G at el. 2018 *Phys. Rev. B* **98** 144307
- [49] Cheng B, Kanda N, Ikeda T N at el. 2020 *Phys. Rev. Lett* **124** 117402
- [50] Cao T, Li Z, and Louie S G 2015 *Phys. Rev. Lett.* **114** 236602
- [51] Seixas L, Rodin A S, Carvalho A, and Castro Neto A H 2016 *Phys. Rev. Lett.* **116** 206803
- [52] Sevinzli H 2017 *Nano Lett.* **17** 258
- [53] Zhang X, Zhu T, Du H at el. 2022 *Phys. Rev. Research* **4**, 033026
- [54] Faist J, Capasso F, Sivco D L at el. 1994 *Science* **264(5158)** 553
- [55] Zhang G P, Bai Y H 2020 *Phys. Rev. B* **101** 081412(R)
- [56] Avetissian H K, Ghazaryan A G, and Mkrtchian G F 2021 *Phys. Rev. B* **104** 125436
- [57] Avchyan B R, Ghazaryan A G, Sargsyan K A, and Sedrakian Kh V 2022 *JETP* **134(2)** 125
- [58] Avchyan B R, Ghazaryan A G, Sargsyan K A, Sedrakian Kh V 2022 *Pis'ma ZETF* **116(7)** 426
- [59] Guclu A D, Potasz P, Korkusinski M, Hawrylak P 2014 *Graphene quantum dot* (Berlin: Springer)
- [60] Avetissian H K, Mkrtchian G F, and Knorr A. 2022 *Phys. Rev. B* **105** 195405
- [61] Avetissian H K, Mkrtchian G F 2022 *Phys. Rev. A* **105** 063504
- [62] Fujita M, Wakabayashi K, Nakada K, and Kusakabe K 1996 *J. Phys. Soc. Jpn.* **65** 1920
- [63] Nakada K, Fujita K, Dresselhaus G, and Dresselhaus M S 1996 *Phys. Rev. B* **54** 17954
- [64] Son Y-W, Cohen M L, and Louie S G 2006 *Phys. Rev. Lett.* **97** 216803
- [65] Ezawa M 2008 *Physica E* **40** 1421
- [66] Ezawa M 2006 *Phys. Rev. B* **73** 045432
- [67] Chu W, Xie Y, Duan S at el. 2010 *Phys. Rev. B* **82** 125301
- [68] Yoon H, Park M, Kim J at el. 2021 *Chem. Phys. Rev.* **2** 031303

- [69] Han M Y, Ozyilmaz B, Zhang Y, and Kim Ph 2007 *Phys. Rev. Lett.* **98** 206805
- [70] Brey L and Fertig H A 2006 *Phys. Rev. B* **73** 235411
- [71] Yamijala Sh, Mukhopadhyay M, and Pati S 2015 *J. Phys. Chem. C* **119**, **21** 12079
- [72] Luryi S, Xu J, Zaslavsky A 2013 *Future trends in microelectronics: Frontiers and innovations* (New York: Wiley)
- [73] Guclu A D, Potasz P, and Hawrylak P 2010 *Phys. Rev. B* **82** 155445
- [74] Feng X, Qin Y, and Liu Y 2018 *Opt. Express* **26** 7132
- [75] Guclu A D, Potasz P, Voznyy O at el. 2009 *Phys. Rev. Lett.* **103** 246805
- [76] Voznyy O, Guclu A D, Potasz P, and Hawrylak P 2011 *Phys. Rev. B* **83** 165417
- [77] Wang W L, Meng S, and Kaxiras E 2008 *Nano Lett.* **8** 241
- [78] Yang L, Cohen M L, and Louie S G 2007 *Nano Lett.* **7** 3112
- [79] Prezzi D, Varsano D, Ruini A at el. 2008 *Phys. Rev. B* **77** 041404
- [80] Prezzi D, Varsano D, Ruini A at el. 2008, and Molinari E 2011 *Phys. Rev. B* **84** 041401
- [81] Murray C B, Kagan C R, and Bawendi M G 2000 *Annu. Rev. Mater. Sci.* **30** 545
- [82] Bera D, Qian L, Tseng T-K, and Holloway P H 2010 *Materials* **3** 2260
- [83] Kumar A, Laux S E, and Stern F 1990 *Phys. Rev. B* **42** 5166
- [84] Ashoori R C, Stormer H L, Weiner J S at el. 1993 *Phys. Rev. Lett.* **71** 613
- [85] Hogege A, Seidl S, Kroner M at el. 2004 *Phys. Rev. Lett.* **93** 217401
- [86] Lewenstein M, Balcou Ph, Ivanov M Yu at el. 1994 *Phys. Rev. A* **49** 2117
- [87] Chen R B, Chang C P, and Lin M F 2010 *Physica E* **42** 2812
- [88] Chang C P, Huang Y C, Lu C L at el. 2006 *Carbon* **44** 508
- [89] Qin Y, Feng X, Liu Y 2019 *Appl. Sci.* **9** 325
- [90] Acharya S, Pashov D, Rudenko A N at el. 2021 *npj Computational Materials* **7** 208
- [91] Wallace P R 1947 *Phys. Rev.* **71** 622
- [92] Zurron-Cifuentes O, Boyero-Garcia R, Hernandez-Garcia C at el. 2019 *Optics Express* **27** 7776
- [93] Avetissian H K, Avchyan B R, and Mkrtchian G F 2012 *J. Phys. B* **45** 025402
- [94] Avetissian H K, Markossian A G, and Mkrtchian G F 2011 *Phys. Rev. A* **84** 013418
- [95] Avetissian H K, Markossian A G, and Mkrtchian G F 2011 *Phys. Lett. A* **375** 3699
- [96] Vampa G, McDonald C R, Orlando G at el. 2014 *Phys. Rev. Lett.* **113** 073901
- [97] Martin R L and Ritchie J P 1993 *Phys. Rev. B* **48** 4845
- [98] Zhang G P 2000 *Phys. Rev. B* **61** 4377